Nuclear transport at full amino-acid resolution

Maurice Dekker, Hendrik W. de Vries, Koen A. Wortelboer, Harm Jan Beekhuis, Erik Van der Giessen, Patrick R. Onck*

Zernike Institute for Advanced Materials, University of Groningen, Groningen, The Netherlands
* Correspondence: p.r.onck@rug.nl

keywords:

Abstract

Recent studies of nuclear pore complexes (NPCs) have provided detailed descriptions of the core scaffold structures, yet fall short in resolving the dynamic FG-meshwork with similar precision. Here, we present a novel modeling framework that enables the simulation of nuclear transport at full amino-acid resolution. We describe the distributions of the different FG-Nups in the central transporter and highlight the dynamic nature of the FG-meshwork, with FG–FG interaction lifetimes on the order of nanoseconds. Our findings reveal that Nsp1, the most abundant FG-Nup in the NPC, creates a central meshwork due to its unique bimodal structure, that is essential for controlling both passive and active transport. By introducing nuclear transport receptors (NTRs)—in the form of Kap95—to the pore, we demonstrate that NTRs play a key role in increasing the energy barrier for translocation of inert particles. We observe a dynamic interplay between high affinity binding to FG-motifs and the temporal fluctuations of the FG-meshwork, leading to local low-density pockets, so-called voids, through which Kaps move. Furthermore, we show that the introduction of Kaps to the FG-meshwork results in a clear “dirty velcro” mechanism with slower Kaps decorating the sticky surface of the high-density GLFG-assembly, thus enabling fast translocation of Kaps through the center of the pore.

Introduction

Nuclear pore complexes (NPCs) regulate the transport of molecules between the nucleus and cytoplasm, ensuring the precise localization of proteins, RNA, and other essential molecules within the cell [1]. NPCs play a pivotal role in maintaining cellular homeostasis, gene expression, and the proper functioning of eukaryotic cells [2]. The permeability barrier of NPCs is highly selective, with non-specific macromolecules only able to efficiently traverse the pore when bound to specific nuclear transport receptors (NTRs). NTRs possess multiple high-affinity binding sites that interact with the FG-motifs in the FG-meshwork. NTRs are considered to be an integral part of the NPC and can dynamically modulate the microenvironment within the pore, in order to allow for fast and efficient translocation [3–6].

NPCs have been extensively studied using cryo-electron tomography and sub-volume averaging across various species, including humans [7–10], yeast [11–16], algae [17] and fungi [18]. These studies provide detailed descriptions of the core scaffold structures, yet fall short in resolving the highly dynamic FG-meshwork due to the dynamic nature of the FG-Nups and transport factors in the central transporter (CT). As a result, the functional organization underlying NPC barrier function and selective nuclear transport remains largely illusive. Super-resolution imaging techniques are able to track NTRs interacting with and transiting through the NPC [19–21], yet do not capture the structural organization of the FG-meshwork during translocation. To unveil the mechanisms underlying NTR translocation, molecular dynamics models have been developed that can act as a "computational microscope", scrutinizing the molecular interactions at the scale of individual FG-Nups and NTRs, and achieving spatial and temporal resolutions that are inaccessible to experiments.

Although atomistic molecular dynamics simulations are a potentially powerful tool to study the key features of nuclear transport on a molecular level, the sheer size and complexity of the NPC and its cargo-complexes limits the applicability of such detailed models to short time and length scales [10, 22]. In order to mitigate these limitations, simplified coarse-grained molecular dynamics models have emerged [23–29], albeit at the cost of smearing out molecular detail and losing the amino-acid footprint characteristic of the highly heterogeneous collection of FG-Nups and NTRs. To resolve this, we have developed an MD model at amino-acid resolution that captures the precise amino-acid sequences of individual FG-Nups, while also encompassing the collective behavior of all FG-Nups in the NPC at experimental timescales [30, 31]. This model has been used by us [32–39] and others [40–42] to study the collective FG-Nup density distribution inside the pore, albeit with transport simulations using rather simplified cargo or Kap models. A comprehensive simulation framework for nucleocytoplasmic transport at amino-acid resolution has been lacking until now, which has hampered a fundamental understanding of the molecular mechanisms underlying selective nuclear transport.

In this work, we present a complete residue-scale model of the yeast NPC, encompassing all $\sim$200 FG-Nups with lengths ranging from 250 to 800 residues, diverse amino acid sequences, and varied protein stoichiometry. Our model includes an amino-acid resolution structural scaffold with precise FG-Nup anchor site locations, and, importantly, a vast collection of Kap95 nuclear transport receptors, also at amino-acid resolution. Large-scale, highly-parallel computations with the model highlight the essential role of Nsp1 in establishing a dynamic permeability barrier through the formation of a dynamic, low-density percolation at the center of the pore, facilitated by highly dynamic FG–FG cross-links with lifetimes of 1 ns. This barrier not only regulates the passage of inert cargo in a size-selective manner, it also facilitates efficient transport through its distinctive FG-rich extended domains that span across the center of the pore. Moreover, our findings underscore the critical role of transport factors in maintaining the NPC's barrier function. Increasing the concentration of Kap95 reinforces the selective properties of the permeability barrier, as suggested by "Kap-centric" models [3–6]. This heightened selectivity arises from two main factors. First of all, the abundance of Kaps in the CT increases the energy barrier for (passive) translocations of inert molecules. Secondly, we find that nuclear transport features a distinct "dirty velcro" mechanism [4, 43], wherein slow Kaps decorate the sticky surface of a high-density GLFG-ring [38], thus allowing for fast Kap translocations through the center of the pore. Finally, our simulations reveal a dynamic transport mechanism wherein Kaps translocate

through transient voids. This mechanism is characterized by the interplay between FG-motif binding and steric hindrance.

Our residue-scale simulation framework for nucleocytoplasmic transport can serve as a computational assay, facilitating the exploration of a broad spectrum of complex problems; from probing the role of variations in pore diameter on nuclear transport, to studying complete RanGTP-controlled bidirectional transport cycles of proteins and RNA.

Results

The yeast NPC at amino-acid resolution

We developed a computational model of the yeast NPC at amino-acid resolution, based on the integrative structure by Kim *et al.* [11]. The model employs our earlier-developed one-bead-per-amino-acid (1BPA) force field for disordered FG-Nups [30, 31, 34–36, 38, 39], that includes residue-specific electrostatic, hydrophobic and cation–π interactions for all twenty amino acids, and comprises backbone potentials that describe the local stiffness of the backbone by discriminating between glycine, proline and other residues. Our model considers the full scaffold structure determined in [11] at near-atomic resolution (Fig. 1a), by placing amino acid beads at each C_α position (Fig. 1b). Furthermore, we included a torus-shaped occlusion to represent the nuclear membrane (Methods). Configurations of undetermined regions in the scaffold Nups, as well as the initial configuration of the FG-Nup meshwork, were generated using a biased self-avoiding random walk (Fig. 1c, Methods). The anchoring locations for each of the disordered FG domains were selected based on the data in [11] (Fig. 1d,e). Since the reference structure did not include sufficient resolution for the nuclear basket proteins Mlp1 and Mlp2 and the corresponding anchoring site of Nup2, these proteins are excluded from the current model. The complete model of the yeast NPC at full amino-acid resolution is illustrated in Fig. 1f.

Structural organization of FG-Nups in the CT

We began by simulating the NPC in the absence of translocating particles. After an extensive equilibration of the FG-meshwork (Methods), we conducted an equilibrium simulation of 5 µs that is used for analysis. We first analyzed the relative localization of the different FG-Nup species in the CT. In the equilibrium state, all GLFG-Nups (Nup116, Nup100, Nup145N, Nup49, and Nup57) coassemble into a high-density, ring-like structure at the center of the NPC (Fig. 2a,b). This "GLFG-ring" forms a high-density barrier that reduces the effective diameter for passive transport (Fig. 2f and Suppl. Fig. S4).

With 48 copies, Nsp1 is the most abundant FG-Nup in the NPC [11]. In the CT, Nsp1 molecules are the only FG-Nups spanning the opening left by the GLFG-ring. The C-terminus of Nsp1 is tethered to the scaffold wall, while the cohesive, collapsed N-terminal domain at the other end dynamically coassembles with the Nups in the GLFG-ring. Consequently, the extended domains of Nsp1, which uniquely feature a high C/H ratio and numerous FG-motifs [38, 44] (Suppl. Fig. S1), span across the central opening of the GLFG-ring (Fig. 2). The eight-fold rotational symmetry of the NPC scaffold results in Nsp1 proteins spanning the CT from multiple directions, creating a low-density yet stable percolated network that efficiently blocks large inert cargoes from translocating across the NPC. Indeed, removal of the FG domains of Nsp1 from the CT significantly lowers the energy barrier for passive translocation (Fig. 2f and Suppl. Fig. S4).

The main interactions stabilizing the FG-Nup assembly in the CT are hydrophobic FG–FG interactions (Fig. 2d), a feature previously observed in FG-Nup condensates as well [38]. Similar to the FG–FG cross-links in FG-Nup condensates, the many FG–FG cross-links in the CT are short-lived, with interaction lifetimes on the order of 1 ns. Interestingly, the composition of the GLFG-ring observed here resembles the GLFG-condensate studied previously [38].

Kap95 proteins coat the GLFG-ring

It has been shown that NTRs can significantly enhance the selectivity of the permeability barrier [6]. However, on a molecular level, the conformational changes of the FG-Nups in response

to high concentrations of transport receptors remain largely elusive. To better understand the localization of transport factors within the NPC and their impact on the selective permeability barrier, we performed a computational titration experiment where we increase the concentration of Kap95 proteins in the CT.

To minimize the re-equilibration time upon introducing a substantial number of translocating particles into the FG-meshwork, we developed a custom pipeline to insert Kap95 proteins into the FG-meshwork by "growing" them at randomly assigned coordinates inside the CT (see Suppl. Methods for more details). We generated five NPC–Kap95 systems with strongly increasing numbers of Kap95 proteins, ranging from a system without Kaps to a system where the FG-meshwork is fully saturated by the Kaps (Fig. 3). This approach allows us to compare the equilibrium dynamics in the CT across a wide range of Kap95 concentrations. From the equilibrium trajectories, we calculated the time-averaged density distributions of the FG-meshwork and the Kap95 proteins (Fig. 3d–f). Notably, we find that the NPC can accommodate a remarkable number of Kap95 proteins; at the highest concentration the NPC can no longer fully accommodate all Kap95 proteins, with up to 120 Kaps in contact with the FG-meshwork. Furthermore, at all Kap95 concentrations, the Kaps primarily localize inside the high-density GLFG-ring, effectively "coating" the GLFG-assembly (Fig. 3f). These interaction regions are consistent with super-resolution microscopy studies in human NPCs [19, 20] and have been associated with the translocation pathway of importins. While the Kap95 proteins tend to occupy areas with a high FG-motif density, their localization is constraint by the high density of the GLFG-ring. As a result, rather than entering the GLFG-assembly, the Kap95 proteins reside around the high-density GLFG-ring where there is a high local FG-motif density but low overall protein density. Increasing the local Kap95 concentration results in a layer of Kaps around the cohesive GLFG-ring, occupying most of the sticky FG-motifs of the GLFG-Nups. As a result, other NTRs experience weaker FG-interactions and become more dynamic, facilitating easier translocation across the NPC [43], mainly by interacting with the central percolation formed by the extended Nsp1 domains. At high Kap95 concentrations, the protein density distributions (Fig. 3d) resemble the hourglass-shaped central plug that is often observed by cryo-EM experiments [11, 14, 16].

Next, we asked how the presence of a large number of Kaps influences the FG-meshwork. Initially, in the absence of Kap95 proteins, the average FG-occupancy, defined as the percentage of FG-motifs cross-linking with another FG-motif, is approximately 40 %, similar to FG-Nup condensates [38]. Surprisingly, the addition of Kap95 proteins does not alter the number of FG–FG cross-linking interactions present in the NPC. Instead, we find a constant number of FG–FG cross-links, independent of the Kap95 concentration, occurring largely in the same regions (Suppl. Fig. S5a and S6). A closer look on the density distribution of the FG-Nups confirms that the FG-meshwork is largely unaffected by the presence of Kap95 proteins (Fig. 3e). This suggests that Kaps do not compete with FG-motifs, but rather bind to the large pool of still available FG-motifs.

For the simulations with 80 and 160 Kaps (and to a lesser degree also the system with 40 Kaps) we noticed an accumulation of Kap95 proteins at the nuclear face of the NPC. Even at these high Kap concentrations, only a few Kaps have dissociated from the FG-meshwork into the nucleoplasm. Instead, the Kaps at the nuclear face of the NPC form a cross-linked mesh together with Nup1. This is consistent with experimental observations of human NPCs where an accumulation of Nup153 (the homologue of Nup1) at the nuclear side has been observed when RanGTP is absent [45, 46]. To account for this, in the next section we implement the effect of RanGTP.

Kaps traverse the pore in multiple discrete steps

To mimic the effect of the Ran-gradient, we have repeated the simulation with 80 Kaps, this time recycling the Kaps that reach the nuclear face of the pore (see Methods for details on the procedure). This recycling procedure induces a moderate flux of Kap95 proteins through the pore, allowing us to study the translocation pathway of Kaps in more detail. Due to the extreme time resolution of our MD simulations versus the millisecond time scale of Kap translocations [47, 48], complete translocation events, i.e. from the cytoplasmic to the nucleoplasmic side, are rare. Yet,

the observed translocation events offer valuable insights into the dynamics of the Kaps within the CT.

In contrast to inert molecules, Kap95 proteins have a high affinity towards the FG-meshwork through the numerous available FG-motifs within the permeability barrier. In the passive equilibration simulations discussed in the previous section, we observed that Kaps tend to populate the regions rich in FG-motifs. Due to these high-affinity interactions, many Kaps are dynamically bound to the surface of the central GLFG-assembly, potentially impeding their diffusive speed. Despite this, the Kaps are not stuck; several Kap95 proteins translocate across the permeability barrier, albeit with largely varying translocation times. An example of such a translocation event is shown in Fig. 4a–f and Suppl. Movie S1. It is remarkable to observe that the Kaps do not move at a constant speed. Instead, they are predominantly confined within their local environment and traverse the pore through many small "jumps" to nearby locations. This confinement is primarily caused by the FG-meshwork and the high-affinity multivalent FG–binding interactions. Therefore, the translocation of Kaps requires two conditions: temporary separation from the FG-motifs to move freely and the presence of openings ("voids") in the meshwork through which the Kap can diffuse. The translocation of Kaps across the CT can be described as a cascade of small random steps without a pronounced overall directionality. The overall directionality is predominalty described by the Ran gradient, off-loading the Kaps when they reach the nuclear face of the pore [49].

A detailed description of a single Kap translocation event (Fig. 4a–f) illustrates this process. The initial contact with the NPC occurs through interactions with the peripheral Nup159 and Nsp1 (Fig. 4d). At this location, the FG-meshwork has a relatively low density, allowing for considerable mobility. Due to the crowding of other Kaps at the cytoplasmic face of the pore (Fig. 3f), the Kap is screened form the sticky FG-interactions of the GLFG-ring, enabling dynamic movement during the first half of this stage. As the Kap progresses, it encounters the cytoplasmically anchored Nup116 (and later also Nup100) (Fig. 4d), leading to an increase in FG-contacts and a subsequent reduction in mobility. The Kap becomes locally confined again (location 2) and dwells for several microseconds at the cytoplasmic face of the pore.

We draw particular attention to the density fluctuations of the FG-meshwork, as depicted in the top row of Fig. 4f. The high dynamics of the FG-meshwork play a crucial role in the Kap's translocation. During the movement from location 2 to 3, the Kap is handed over to the other side of the pore. Notably, an opening (void) in the center of the pore (Fig. 4f-3) allows the Kap to slide over the GLFG surface towards the nuclear face of the pore. After detaching completely from the GLFG-ring, the Kap moves to the opposite side of the pore, primarily driven by interactions with Nsp1.

In the final phase, the Kap gets temporarily stuck on the GLFG-ring due to numerous additional interactions with Nup57 (and Nup49), while interactions with Nsp1 are reduced. This reduced mobility lasts for several microseconds until the interactions with Nup57 are disrupted, and the Kap detaches from the GLFG-ring. Finally, guided by Nsp1 on the nuclear face, the Kap diffuses down and is "removed" from the CT (location 5). This detailed observation of a single Kap translocation event highlights the intricate and dynamic nature of nuclear transport, emphasizing the crucial role of FG-motifs and the dynamic FG-meshwork in facilitating efficient and selective translocation through the NPC.

To further illustrate how interactions with the GLFG-ring impact the mobility of translocating Kaps, we compared the distribution of "slow" and "fast" Kaps (Fig. 4g). These density distributions reveal that the highest Kap dynamics is observed at the cytoplasmic face of the pore, where the FG-meshwork is relatively sparse and the Kaps are mostly interacting with Nup159 and Nsp1 (Fig. 4d).The relatively slower Kaps are primarily found along the surface of the GLFG-ring, where their mobility is reduced by the many FG–binding interactions. Notably, these slower Kaps screen other Kaps from the sticky FG-interactions of the GLFG-ring, facilitating rapid transport through the pore center. This indicates that while the FG-meshwork facilitates initial Kap interactions and mobility, the denser GLFG regions act as checkpoints, slowing down some Kaps to enable faster translocation for others due to reduced FG-binding [49].

Discussion

Dynamic architecture of the CT

We have developed a residue-scale molecular dynamics framework for nuclear transport in the yeast NPC to study the conformational changes of the permeability barrier during NTR translocation. We used this framework to study the yeast NPC under drastically varying Kap95 concentrations, starting from an NPC devoid of NTRs. Our simulations revealed a large variation in protein density in the pore's permeability barrier. Specifically, the cohesive GLFG-Nups form a ring-like assembly at the scaffold surface, that is sustained by numerous, highly dynamic FG–FG cross-links. The opening left by this GLFG-ring is filled with a low-density, percolated network of Nsp1 proteins. Due to their unique bimodal nature—containing both a 200-residue cohesive domain and a 400-residue noncohesive, extended domain, both encompassing many FG-motifs—Nsp1 proteins are able to span across the central pore opening, with the C-terminal anchored to the NPC scaffold and the cohesive N-terminal domain dynamically co-assembling with the GLFG-Nups that surround the inner scaffold surface. The many FG-motifs in the extended domains of Nsp1 establish a cross-linked yet dynamic percolation at the center of the pore, acting as a size-selective filter for inert molecules [42]. Furthermore, these FG-motifs play a crucial role in NTR translocations as upon removal of only the FG–Kap95 interactions in the extended domain, all transport is eliminated. It is noteworthy that the extended domain of Nsp1, the only FG domain combining low cohesivity with regular FG-motif spacing, plays such a crucial role in nuclear transport.

The GLFG-ring at the center of the CT has multiple functions. First of all, it acts as a seal between the pore scaffold and the central, low-density Nsp1 percolated network, preventing any leakage of molecules along the scaffold surface. Secondly, the GLFG-condensate acts as a dynamic anchoring location for the cohesive Nsp1 domains, thus enabling the extended domains of Nsp1 to span the central pore opening. This second "anchor" of the extended Nsp1 domains is critical to retain the Nsp1 percolation at the center of the pore, as without it, most of the Nsp1-proteins would be expelled from the pore [37, 38].

The dynamic nature of the FG–FG cross-links in the GLFG-ring and the Nsp1-network at the center of the pore increase the flexibility of the permeability barrier, allowing it to function under varying pore diameters [7, 13, 14] and transport large cargoes [28, 50–52] without losing its selective properties.

NPC permeability barrier as an FG phase condensate

Experimental and computational studies have shown that the FG domains of several FG-Nups phase separate and form biomolecular condensates [38, 53–56] that are stabilized by a high degree of dynamic FG–FG cross-linking [38]. Our observations reveal an intriguing resemblance between these FG-Nup condensates and the high-density GLFG-ring in the CT. Both assemblies exhibit a highly dynamic percolated network with a similar degree of FG–FG cross-linking and similar dynamics of these cross-links. These properties remain largely unaffected by the partitioning of Kap95 in the CT, with only minor differences observed in the distribution of FG–FG cross-links between NPCs without Kaps and those with high concentrations of Kap95.

Despite the extensive cross-linking, the FG-meshwork remains highly dynamic due to the characteristic "stickers-and-spacers" architecture of FG-Nups. Cohesive FG-motifs (stickers) drive the formation of a percolated network at the center of the pore, while FG-spacers (primarily consisting of polar and charged amino acids) mediate the contacts among these stickers [38, 56, 57]. This results in a dynamic FG-meshwork where the sticky FG-motif interactions are modulated by the hydrophilic character of the FG-spacers.

Although the ring-like GLFG-assembly cannot be strictly termed a phase condensate—since the FG-Nups cannot freely diffuse due to their tethering to the NPC scaffold [58, 59]—the similarity between the NPC's GLFG-assembly and FG-Nup condensates is striking. In our previous work [38], we studied the phase separation of an FG-Nup mixture resembling the stoichiometry of the NPC. Here, the central GLFG-Nups (Nup100, Nup116, Nup145N, Nup49 and Nup57)

undergo co-condensation and form one large GLFG-Nup condensate, while the peripheral FG-Nups (Nup159, Nup1 and Nup60) exclusively remained in the dilute phase. Interestingly, a small fraction (10 %) of Nsp1 was found to co-condensate with the GLFG-Nups as well, primarily interacting through its cohesive N-terminal domain. This isolated "NPC condensate" has a striking resemblance with the organization of the FG-meshwork in the NPC, wherein the GLFG-Nups dynamically co-assemble into a ring-like structure and where the cohesive N-terminal domain of Nsp1 co-assembles with the GLFG-Nups. Although the FG-meshwork inside the NPC is tethered to the pore scaffold, both assemblies have comparable protein densities of approximately 400 mg/mL, contain the same co-condensation of five GLFG-Nups (Nup100, Nup116, Nup145N, Nup49 and Nup57), and are stabilized by a large number of dynamic FG–FG cross-links. Regardless of all these similarities, the key difference between FG condensates and the CT is the tethered nature of Nsp1, allowing its extended domain to play a decisive role in the NPC's size-selective permeability barrier.

Nsp1 as a phase state regulator in the NPC

Nsp1 has been identified as a phase state regulator for FG-Nup condensates in vitro [60]. In those studies, the cohesive N-terminal domains of Nsp1 co-condensate with GLFG-Nups, while the extended domains are projected from the condensate surface. Our simulations reveal a similar behavior: the cohesive domains of Nsp1 dynamically co-assemble with the GLFG-ring, while the noncohesive extended domains are projected towards the center of the pore. This suggests that Nsp1 may also play a phase regulatory role in the NPC, keeping the FG-Nups in a more dynamic state. By doing so, Nsp1 prevents the potential aggregation of FG-Nups into rigid beta-structures, thereby contributing to the robustness and stability of the permeability barrier.

Kaps reinforce the selective permeability barrier

Our results support the Kap-centric models, which posit that Kaps are essential components of the selective permeability barrier [3–6]. At low Kap concentrations, the Kap95 proteins primarily localize around the GLFG-ring, effectively reducing the pore's diameter and thereby limiting the leakage of unwanted molecules. At higher Kap concentrations, more Kap95 proteins not only localize around the GLFG-ring but also disperse throughout the entire FG-meshwork. Interestingly, the availability of FG-motifs is not the limiting factor; instead, the available space at the center of the pore becomes depleted. With increasing concentrations of Kap95, the permeability barrier becomes more size-selective. The energy barrier for passive translocation of large inert particles (greater than 3.0 nm) is significantly increased, while the passive translocation of small inert particles (less than 1.5 nm) remains largely unaffected. This reinforces the concept that Kaps enhance the NPC's ability to selectively filter macromolecules based on size.

Kaps traverse the CT via a "dirty velcro" mechanism

Kap translocations are predominantly non-directional [61]. Without the Ran-gradient, a net flux of NTR translocations is absent. This is also translated to our simulations: without active removal of Kaps from the nuclear face of the NPC, almost all Kaps remain inside the CT, moving equally in both directions. Only when a Ran-gradient was mimicked, we observed a net movement towards the nuclear side of the pore.

Our findings reveal that Kaps do not translocate across the pore in a continuous motion. Instead, they display significant variations in speed during translocation, influenced by their interactions with various components of the CT. Specifically, Kaps experience changes in their mobility based on their location within the pore: those interacting extensively with the GLFG-ring exhibit reduced mobility, while Kaps translocating through the center of the pore move more rapidly. This cooperative behavior among Kaps increases the efficiency of translocations [26]. This also suggests that there are not two distinct populations of fast and slow Kaps, or at least these two populations are interchangeable. All Kaps dwell at several locations in the CT (e.g. cytoplasmic face, GLFG-center, nucleoplasmic face), temporarily screening the sticky FG-interactions for other Kaps. This indicates that crowding of Kaps actually benefits rapid translocation, a phenomenon

previously demonstrated by Zheng et al. [26].

Our simulations provided a comprehensive picture of nuclear transport into the cell nucleus. Both passive and NTR-driven transport occur primarily through the center of the pore, where protein density is relatively low, and the occurrence of voids through which particles can dynamically translocate is high. The NTRs translocate via a “dirty velcro” mechanism [4, 43], wherein a volume of Kaps shield other Kaps from the sticky FG-interactions of the FG-meshwork. This shielding effect allows for more efficient translocation through the pore center.

In summary, the dynamic interplay between the Kaps’ slow and fast states, combined with the density fluctuations of the FG-meshwork, underpins a highly efficient and selective nuclear transport mechanism. Our residue-scale modeling and simulations underscore the importance of the “dirty velcro” mechanism, where the collective behavior of Kaps facilitates rapid and selective transport through the nuclear pore complex.

Methods

Residue-scale model for intrinsically disordered proteins

All molecular dynamics simulations are performed using the 1BPA-1.1 model for intrinsically disordered proteins [38]. In this implicit-solvent coarse-grained model each amino acid is represented by a single interacting bead, carrying residue-specific physicochemical properties (charge and hydrophobicity) and calibrated to accurately reproduce experimentally determined hydrodynamic radii over a range of yeast FG-Nup segments [31, 38]. The 1BPA model incorporates a sequence-specific backbone stiffness by distinguishing between three groups of amino acids (i.e. glycine, proline and other residues) [30]. Furthermore, cation–pi interactions are included by recalibrating the interaction potentials between cationic (R,K) and aromatic (F,Y,W) residues [34].

All simulations are performed using GROMACS [62] molecular dynamics software (version 2019.6), where the stochastic dynamics integrator operates with a time step of 0.02 ps and inverse friction coefficient γ^{-1} = 50 ps. Simulations are performed at 300 K and physiological salt concentration of 150 mM by setting the Debye screening constant κ = 1.27 nm^{-1}.

Residue-scale model of yeast Kap95

For the residue-scale model of yeast Kap95, we used our previously developed model [37] of the unbound state of Kap95 (PDB ID: 3ND2 [63]). The Kaps are modeled as inert proteins, where the secondary and tertiary structure are maintained using an elastic network. Multivalent interactions with FG-Nups are largely preserved by introducing specific FG–binding site interactions and by using the 1BPA electrostatic and cation–pi interactions. The ten binding sites per Kap95 are accurately determined and refined from a computational study [64]. See Supplementary Methods and Ref. [37] for more details on the CG model and calibration procedure.

Generation of residue-scale model of the yeast NPC

The structural model of the yeast NPC was derived from an integrative structure of an isolated NPC obtained by Kim *et al.* [11]. The origin of the coordinate system was chosen to coincide with the center of mass of the scaffold structure. Multi-resolution (C_α or coarser) PDB structures were then exported for all individual scaffold Nups and FG-Nup domains that comprise the eightfold symmetric NPC structure. When available, the C_α-positions were extracted and stored for each Nup, with the exclusion of nuclear basket proteins Mlp1, Mlp2 and Nup2, membrane ring Nups Pom33, Pom34 and Ndc1, and the cytoplasm-facing Gle1 (see Suppl. Tab. S1 for an overview of all modeled scaffold proteins). Missing residues or flexible linker regions between folded domains were positioned via a self-avoiding random walk (see Suppl. Methods), thus completing the scaffold structure to the extent possible. The scaffold structure was fixed in space by freezing all non-linker scaffold residues (i.e. their position was not updated during the simulations). Interactions between scaffold residues and disordered FG domains only comprise excluded volume interactions.

A half-open torus-shaped occlusion was then inserted to mimic the nuclear membrane. The minor and major radii of the torus were set to 13.25 nm and 55.5 nm, respectively (Fig. 1f). This is in accordance with constraints used in the integrative modeling underlying the NPC structure [11]. The sterically inert beads that constitute the torus-shaped membrane were given a diameter of 3.0 nm and only interact with the disordered FG domains by means of volume exclusion. Interactions between the torus-shaped occlusion and the flexible linkers or frozen scaffold beads were excluded.

The β-propellers of Nup159 (residues 1–382) were included in the model and attached to the disordered FG domain (residues 382–1116). The structure of the β-propeller was preserved by applying a network of harmonic bonds, where harmonic bonds with spring constant k = 8000 kJ mol^{-1} nm^{-2} were applied to any non-neighboring residues with a separation smaller than 1.2 nm. Other studies on the stoichiometry of NPC components [65] indicated that a second copy of Nup1 is likely present, in addition to the structure of Kim *et al.* adapted here. A second copy of Nup1 was therefore added, with the same anchoring coordinates as the first copy of Nup1 (see Suppl. Methods).

Passive equilibration simulations

Following the generation of the FG-meshwork, an extensive equilibration simulation of 2.5×10^8 steps (5 µs) of the complete NPC (in the absence of Kaps) such that the FG-meshwork could homogenize before the 2.5×10^8 steps (5 µs) production run. Following the initial equilibration of the FG-meshwork, Kap95 proteins were inserted into the NPC using a custom "growing" pipeline (see Suppl. Methods for more details). After the insertion of the desired number of Kaps, another equilibration run of 2.5×10^8 steps (5 µs) was performed to allow the NPC–Kap systems to reach a new equilibrium state before the 2.5×10^8 steps (5 µs) production run.

Kap95 recycling simulations

To simulate the effect of a Ran-gradient, we implemented a recycling process for Kap95 proteins upon reaching the nuclear side of the NPC. Every 5.0×10^5 steps (10 ns) the simulation is paused and the center-of-mass (COM) position of each Kap is determined. If the z-coordinate of a Kap is found to be 20 nm below the center of the NPC scaffold, the Kap is deemed to have reached the nuclear side of the pore (Suppl. Fig. S8). The identified Kap is then removed from the nuclear side of the FG-meshwork and reinserted at the cytoplasmic side ($z_{\mathrm{COM}} = -60$ nm). After checking and recycling all Kaps, the simulation is continued. This procedure is continued until an aggregate simulation trajectory of 1×10^9 simulation steps (20 µs) is obtained.

Interaction lifetime analysis

Distributions of residue–residue contact lifetimes are calculated using a transition-based or core-state approach [66, 67], where two separate cut-offs are used to define the formation and breaking of a contacts between two residues. The original analysis method was developed for all-atom molecular systems [66]. To apply this analysis to coarse-grained systems, we have scaled the all-atom cut-offs for formation and breaking to $r_{\mathrm{form,CG}}$ = 0.55 nm and $r_{\mathrm{break,CG}}$ = 1.2 nm for 1BPA simulations. To verify the robustness of the chosen cut-off values, we compared the contact lifetime distributions for various combinations of cut-off parameters and found no significant difference when changing the either of the cut-offs by 10 % (Suppl. Fig. **??**).

Void analysis and PMF barriers

Energy barriers for passive translocation of inert cargo are calculated using the void analysis method described by Winogradoff et al. [42]. The simulation volume was mapped onto a 3D grid, with a grid size of 6 Å. For each configuration of the FG-meshwork, we assessed whether a spherical probe of radius r_{p} could be placed at the center of each voxel without overlapping with any amino acid bead of the meshwork or the pore scaffold. The resulting 3D void maps were then converted into 1D potential occupancy maps by calculating the percentage of available

voxels in each slice along the pore axis. This potential occupancy function was calculated every 5×10^4 steps (1 ns) of the equilibrium trajectory. The average potential occupancy function over the trajectory was then transformed into an effective PMF curve using Boltzmann inversion. We refer the reader to Ref. [42] for more details on the analysis procedure. The analysis was performed with the codes provided by the paper, with a custom constraint to exclude the volume of the nuclear membrane from the void analysis.

To evaluate the pathway for passive translocation through the CT, we determined the time-averaged distribution of the "voids" within the pore. This was done by computing the 3D void map for each instantaneous configuration of the CT and then averaging these maps over the simulation time. The resulting time-averaged void map represents the probability that each voxel can accommodate an inert protein with radius r_p. Subsequently, this 3D void map was averaged circumferentially around the pore's axis to produce a 2D void map in (r, z) coordinates, as shown in Fig. 4h.

Acknowledgements

This work was financially supported by the Netherlands Organization of Scientific Research grant no. OCENW.GROOT.2019.068. This work made use of the Dutch national e-infrastructure with the support of the SURF Cooperative using grant nos. EINF-3563 and EINF-6556. We thank the Center for Information Technology of the University of Groningen for their support and for providing access to the Hábrók high performance computing cluster.

References

1. Tran, E.J.; Wente, S.R. Dynamic Nuclear Pore Complexes: Life on the Edge. *Cell* **2006**, *125*, 1041–1053. doi:10.1016/j.cell.2006.05.027.
2. Strambio-De-Castillia, C.; Niepel, M.; Rout, M.P. The nuclear pore complex: bridging nuclear transport and gene regulation. *Nature Reviews Molecular Cell Biology* **2010**, *11*, 490–501. doi:10.1038/nrm2928.
3. Kapinos, L.E.; Schoch, R.; Wagner, R.; Schleicher, K.D.; Lim, R.Y. Karyopherin-Centric Control of Nuclear Pores Based on Molecular Occupancy and Kinetic Analysis of Multivalent Binding with FG Nucleoporins. *Biophysical Journal* **2014**, *106*, 1751–1762. doi:10.1016/j.bpj.2014.02.021.
4. Lim, R.Y.; Huang, B.; Kapinos, L.E. How to operate a nuclear pore complex by Kap-centric control. *Nucleus* **2015**, *6*, 366–372. doi:10.1080/19491034.2015.1090061.
5. Kapinos, L.E.; Huang, B.; Rencurel, C.; Lim, R.Y. Karyopherins regulate nuclear pore complex barrier and transport function. *Journal of Cell Biology* **2017**, *216*, 3609–3624. doi:10.1083/jcb.201702092.
6. Kalita, J.; Kapinos, L.E.; Zheng, T.; Rencurel, C.; Zilman, A.; Lim, R.Y. Karyopherin enrichment and compensation fortifies the nuclear pore complex against nucleocytoplasmic leakage. *Journal of Cell Biology* **2022**, *221*. doi:10.1083/jcb.202108107.
7. Schuller, A.P.; Wojtynek, M.; Mankus, D.; Tatli, M.; Kronenberg-Tenga, R.; Regmi, S.G.; Dip, P.V.; Lytton-Jean, A.K.R.; Brignole, E.J.; Dasso, M.; et al. The cellular environment shapes the nuclear pore complex architecture. *Nature* **2021**, *598*, 667–671. doi:10.1038/s41586-021-03985-3.
8. Petrovic, S.; Samanta, D.; Perriches, T.; Bley, C.J.; Thierbach, K.; Brown, B.; Nie, S.; Mobbs, G.W.; Stevens, T.A.; Liu, X.; et al. Architecture of the linker-scaffold in the nuclear pore. *Science* **2022**, *376*. doi:10.1126/science.abm9798.
9. Bley, C.J.; Nie, S.; Mobbs, G.W.; Petrovic, S.; Gres, A.T.; Liu, X.; Mukherjee, S.; Harvey, S.; Huber, F.M.; Lin, D.H.; et al. Architecture of the cytoplasmic face of the nuclear pore. *Science* **2022**, *376*. doi:10.1126/science.abm9129.
10. Mosalaganti, S.; Obarska-Kosinska, A.; Siggel, M.; Taniguchi, R.; Turoňová, B.; Zimmerli, C.E.; Buczak, K.; Schmidt, F.H.; Margiotta, E.; Mackmull, M.T.; et al. AI-based structure prediction empowers integrative structural analysis of human nuclear pores. *Science* **2022**, *376*. doi:10.1126/science.abm9506.
11. Kim, S.J.; Fernandez-Martinez, J.; Nudelman, I.; Shi, Y.; Zhang, W.; Raveh, B.; Herricks, T.; Slaughter, B.D.; Hogan, J.A.; Upla, P.; et al. Integrative structure and functional anatomy of a nuclear pore complex. *Nature* **2018**, *555*, 475–482. doi:10.1038/nature26003.
12. Allegretti, M.; Zimmerli, C.E.; Rantos, V.; Wilfling, F.; Ronchi, P.; Fung, H.K.H.; Lee, C.W.; Hagen, W.; Turoňová, B.; Karius, K.; et al. In-cell architecture of the nuclear pore and snapshots of its turnover. *Nature* **2020**, *586*, 796–800. doi:10.1038/s41586-020-2670-5.
13. Zimmerli, C.E.; Allegretti, M.; Rantos, V.; Goetz, S.K.; Obarska-Kosinska, A.; Zagoriy, I.; Halavatyi, A.; Hummer, G.; Mahamid, J.; Kosinski, J.; et al. Nuclear pores dilate and constrict in cellulo. *Science* **2021**, *374*, eabd9776. doi:10.1126/science.abd9776.

14. Akey, C.W.; Singh, D.; Ouch, C.; Echeverria, I.; Nudelman, I.; Varberg, J.M.; Yu, Z.; Fang, F.; Shi, Y.; Wang, J.; et al. Comprehensive structure and functional adaptations of the yeast nuclear pore complex. *Cell* **2022**, *185*, 361–378. doi:10.1016/j.cell.2021.12.015.
15. Li, Z.; Chen, S.; Zhao, L.; Huang, G.; Pi, X.; Sun, S.; Wang, P.; Sui, S.F. Near-atomic structure of the inner ring of the Saccharomyces cerevisiae nuclear pore complex. *Cell Research* **2022**, *32*, 437–450. doi:10.1038/s41422-022-00632-y.
16. Akey, C.W.; Echeverria, I.; Ouch, C.; Nudelman, I.; Shi, Y.; Wang, J.; Chait, B.T.; Sali, A.; Fernandez-Martinez, J.; Rout, M.P. Implications of a multiscale structure of the yeast nuclear pore complex. *Molecular Cell* **2023**, *83*, 3283–3302. doi:10.1016/j.molcel.2023.08.025.
17. Mosalaganti, S.; Kosinski, J.; Albert, S.; Schaffer, M.; Strenkert, D.; Salomé, P.A.; Merchant, S.S.; Plitzko, J.M.; Baumeister, W.; Engel, B.D.; et al. In situ architecture of the algal nuclear pore complex. *Nature Communications* **2018**, *9*, 2361. doi:10.1038/s41467-018-04739-y.
18. Lin, D.H.; Stuwe, T.; Schilbach, S.; Rundlet, E.J.; Perriches, T.; Mobbs, G.; Fan, Y.; Thierbach, K.; Huber, F.M.; Collins, L.N.; et al. Architecture of the symmetric core of the nuclear pore. *Science* **2016**, *352*. doi:10.1126/science.aaf1015.
19. Ma, J.; Goryaynov, A.; Sarma, A.; Yang, W. Self-regulated viscous channel in the nuclear pore complex. *Proceedings of the National Academy of Sciences* **2012**, *109*, 7326–7331. doi:10.1073/pnas.1201724109.
20. Ma, J.; Goryaynov, A.; Yang, W. Super-resolution 3D tomography of interactions and competition in the nuclear pore complex. *Nature Structural & Molecular Biology* **2016**, *23*, 239–247. doi:10.1038/nsmb.3174.
21. Chowdhury, R.; Sau, A.; Musser, S.M. Super-resolved 3D tracking of cargo transport through nuclear pore complexes. *Nature Cell Biology* **2022**, *24*, 112–122. doi:10.1038/s41556-021-00815-6.
22. Miao, L.; Schulten, K. Transport-Related Structures and Processes of the Nuclear Pore Complex Studied through Molecular Dynamics. *Structure* **2009**, *17*, 449–459. doi:10.1016/j.str.2008.12.021.
23. Moussavi-Baygi, R.; Jamali, Y.; Karimi, R.; Mofrad, M.R.K. Brownian Dynamics Simulation of Nucleocytoplasmic Transport: A Coarse-Grained Model for the Functional State of the Nuclear Pore Complex. *PLoS Computational Biology* **2011**, *7*, e1002049. doi:10.1371/journal.pcbi.1002049.
24. Tagliazucchi, M.; Peleg, O.; Kröger, M.; Rabin, Y.; Szleifer, I. Effect of charge, hydrophobicity, and sequence of nucleoporins on the translocation of model particles through the nuclear pore complex. *Proceedings of the National Academy of Sciences of the United States of America* **2013**, *110*, 3363–8. doi:10.1073/pnas.1212909110.
25. Huang, K.; Tagliazucchi, M.; Park, S.H.; Rabin, Y.; Szleifer, I. Nanocompartmentalization of the Nuclear Pore Lumen. *Biophysical Journal* **2020**, *118*, 219–231. doi:10.1016/j.bpj.2019.11.024.
26. Zheng, T.; Zilman, A. Self-regulation of the nuclear pore complex enables clogging-free crowded transport. *Proceedings of the National Academy of Sciences* **2023**, *120*. doi:10.1073/pnas.2212874120.
27. Yu, M.; Heidari, M.; Mikhaleva, S.; Tan, P.S.; Mingu, S.; Ruan, H.; Reinkemeier, C.D.; Obarska-Kosinska, A.; Siggel, M.; Beck, M.; et al. Visualizing the disordered nuclear transport machinery in situ. *Nature* **2023**. doi:10.1038/s41586-023-05990-0.
28. Hudait, A.; Voth, G.A. HIV-1 capsid shape, orientation, and entropic elasticity regulate translocation into the nuclear pore complex. *Proceedings of the National Academy of Sciences* **2024**, *121*. doi:10.1073/pnas.2313737121.
29. Zheng, T.; Zilman, A. Kinetic cooperativity resolves bidirectional clogging within the nuclear pore complex. *Biophysical Journal* **2024**. doi:10.1016/j.bpj.2024.03.027.
30. Ghavami, A.; Van der Giessen, E.; Onck, P.R. Coarse-grained potentials for local interactions in unfolded proteins. *Journal of Chemical Theory and Computation* **2013**, *9*, 432–440. doi:10.1021/ct300684j.
31. Ghavami, A.; Veenhoff, L.; Van der Giessen, E.; Onck, P.R. Probing the disordered domain of the nuclear pore complex through coarse-grained molecular dynamics simulations. *Biophysical Journal* **2014**, *107*, 1393–1402. doi:10.1016/j.bpj.2014.07.060.
32. Popken, P.; Ghavami, A.; Onck, P.R.; Poolman, B.; Veenhoff, L.M. Size-dependent leak of soluble and membrane proteins through the yeast nuclear pore complex. *Molecular Biology of the Cell* **2015**, *26*, 1386–1394. doi:10.1091/mbc.E14-07-1175.
33. Ghavami, A.; Van der Giessen, E.; Onck, P.R. Energetics of transport through the nuclear pore complex. *PLoS ONE* **2016**, *11*, 1–13. doi:10.1371/journal.pone.0148876.
34. Jafarinia, H.; Van der Giessen, E.; Onck, P.R. Phase separation of toxic dipeptide repeat proteins related to C9orf72 ALS/FTD. *Biophysical Journal* **2020**, *119*, 843–851. doi:10.1016/j.bpj.2020.07.005.
35. Fragasso, A.; de Vries, H.W.; Andersson, J.; van der Sluis, E.O.; Van der Giessen, E.; Dahlin, A.; Onck, P.R.; Dekker, C. A designer FG-Nup that reconstitutes the selective transport barrier of the nuclear pore complex. *Nature Communications* **2021**, *12*, 2010. doi:10.1038/s41467-021-22293-y.
36. Jafarinia, H.; Van der Giessen, E.; Onck, P.R. Molecular basis of C9orf72 poly-PR interference with the β-karyopherin family of nuclear transport receptors. *Scientific Reports* **2022**, *12*, 21324. doi:10.1038/s41598-022-25732-y.
37. Fragasso, A.; de Vries, H.W.; Andersson, J.; van der Sluis, E.O.; Van der Giessen, E.; Onck, P.R.; Dekker, C. Transport receptor occupancy in nuclear pore complex mimics. *Nano Research* **2022**, *15*, 9689–9703. doi:10.1007/s12274-022-4647-1.
38. Dekker, M.; Van der Giessen, E.; Onck, P.R. Phase separation of intrinsically disordered FG-Nups is driven by highly dynamic FG motifs. *Proceedings of the National Academy of Sciences* **2023**, *120*.

doi:10.1073/pnas.2221804120.
39. Jafarinia, H.; van der Giessen, E.; Onck, P.R. C9orf72 polyPR directly binds to various nuclear transport components. *eLife* **2024**, *12*. doi:10.7554/eLife.89694.
40. Peyro, M.; Soheilypour, M.; Ghavami, A.; Mofrad, M.R.K. Nucleoporin's Like Charge Regions Are Major Regulators of FG Coverage and Dynamics Inside the Nuclear Pore Complex. *PLOS ONE* **2015**, *10*, e0143745. doi:10.1371/journal.pone.0143745.
41. Peyro, M.; Dickson, A.M.; Mofrad, M.R.K. Nucleoporins' exclusive amino acid sequence features regulate their transient interaction with and selectivity of cargo complexes in the nuclear pore. *Molecular Biology of the Cell* **2021**, *32*. doi:10.1091/mbc.E21-04-0161.
42. Winogradoff, D.; Chou, H.Y.; Maffeo, C.; Aksimentiev, A. Percolation transition prescribes protein size-specific barrier to passive transport through the nuclear pore complex. *Nature Communications* **2022**, *13*, 5138. doi:10.1038/s41467-022-32857-1.
43. Schleicher, K.D.; Dettmer, S.L.; Kapinos, L.E.; Pagliara, S.; Keyser, U.F.; Jeney, S.; Lim, R.Y. Selective transport control on molecular velcro made from intrinsically disordered proteins. *Nature Nanotechnology* **2014**, *9*, 525–530. doi:10.1038/nnano.2014.103.
44. Yamada, J.; Phillips, J.L.; Patel, S.; Goldfien, G.; Calestagne-Morelli, A.; Huang, H.; Reza, R.; Acheson, J.; Krishnan, V.V.; Newsam, S.; et al. A Bimodal Distribution of Two Distinct Categories of Intrinsically Disordered Structures with Separate Functions in FG Nucleoporins. *Molecular & Cellular Proteomics* **2010**, *9*, 2205–2224. doi:10.1074/mcp.M000035-MCP201.
45. Görlich, D.; Panté, N.; Kutay, U.; Aebi, U.; Bischoff, F.R. Identification of different roles for RanGDP and RanGTP in nuclear protein import. *The EMBO Journal* **1996**, *15*, 5584–5594. doi:10.1002/j.1460-2075.1996.tb00943.x.
46. Lowe, A.R.; Tang, J.H.; Yassif, J.; Graf, M.; Huang, W.Y.; Groves, J.T.; Weis, K.; Liphardt, J.T. Importin-β modulates the permeability of the nuclear pore complex in a Ran-dependent manner. *eLife* **2015**, *4*. doi:10.7554/eLife.04052.
47. Yang, W.; Gelles, J.; Musser, S.M. Imaging of single-molecule translocation through nuclear pore complexes. *Proceedings of the National Academy of Sciences* **2004**, *101*, 12887–12892. doi:10.1073/pnas.0403675101.
48. Yang, W.; Musser, S.M. Nuclear import time and transport efficiency depend on importin β concentration. *Journal of Cell Biology* **2006**, *174*, 951–961. doi:10.1083/jcb.200605053.
49. Lowe, A.R.; Siegel, J.J.; Kalab, P.; Siu, M.; Weis, K.; Liphardt, J.T. Selectivity mechanism of the nuclear pore complex characterized by single cargo tracking. *Nature* **2010**, *467*, 600–603. doi:10.1038/nature09285.
50. Paci, G.; Zheng, T.; Caria, J.; Zilman, A.; Lemke, E.A. Molecular determinants of large cargo transport into the nucleus. *eLife* **2020**, *9*, 1–24. doi:10.7554/eLife.55963.
51. Zila, V.; Margiotta, E.; Turoňová, B.; Müller, T.G.; Zimmerli, C.E.; Mattei, S.; Allegretti, M.; Börner, K.; Rada, J.; Müller, B.; et al. Cone-shaped HIV-1 capsids are transported through intact nuclear pores. *Cell* **2021**, *184*, 1032–1046. doi:10.1016/j.cell.2021.01.025.
52. Li, Z.; Chen, S.; Zhao, L.; Huang, G.; Xu, H.; Yang, X.; Wang, P.; Gao, N.; Sui, S.F. Nuclear export of pre-60S particles through the nuclear pore complex. *Nature* **2023**, *618*, 411–418. doi:10.1038/s41586-023-06128-y.
53. Schmidt, H.B.; Görlich, D. Nup98 FG domains from diverse species spontaneously phase-separate into particles with nuclear pore-like permselectivity. *eLife* **2015**, *4*, 1–30. doi:10.7554/eLife.04251.
54. Celetti, G.; Paci, G.; Caria, J.; VanDelinder, V.; Bachand, G.; Lemke, E.A. The liquid state of FG-nucleoporins mimics permeability barrier properties of nuclear pore complexes. *Journal of Cell Biology* **2020**, *219*. doi:10.1083/jcb.201907157.
55. Najbauer, E.E.; Ng, S.C.; Griesinger, C.; Görlich, D.; Andreas, L.B. Atomic resolution dynamics of cohesive interactions in phase-separated Nup98 FG domains. *Nature Communications* **2022**, *13*, 1494. doi:10.1038/s41467-022-28821-8.
56. Ng, S.C.; Biswas, A.; Huyton, T.; Schünemann, J.; Reber, S.; Görlich, D. Barrier properties of Nup98 FG phases ruled by FG motif identity and inter-FG spacer length. *Nature Communications* **2023**, *14*, 747. doi:10.1038/s41467-023-36331-4.
57. Martin, E.W.; Holehouse, A.S.; Peran, I.; Farag, M.; Incicco, J.J.; Bremer, A.; Grace, C.R.; Soranno, A.; Pappu, R.V.; Mittag, T. Valence and patterning of aromatic residues determine the phase behavior of prion-like domains. *Science* **2020**, *367*, 694–699. doi:10.1126/science.aaw8653.
58. Kozai, T.; Fernandez-Martinez, J.; van Eeuwen, T.; Gallardo, P.; Kapinos, L.E.; Mazur, A.; Zhang, W.; Tempkin, J.; Panatala, R.; Delgado-Izquierdo, M.; et al. Dynamic molecular mechanism of the nuclear pore complex permeability barrier. *bioRxiv* **2023**. doi:10.1101/2023.03.31.535055.
59. Cowburn, D.; Rout, M. Improving the hole picture: towards a consensus on the mechanism of nuclear transport. *Biochemical Society Transactions* **2023**, *51*, 871–886. doi:10.1042/BST20220494.
60. Otto, T.A.; Bergsma, T.; Dekker, M.; Mouton, S.N.; Gallardo, P.; Wolters, J.C.; Steen, A.; Onck, P.R.; Veenhoff, L.M. Nucleoporin Nsp1 surveils the phase state of FG-Nups. *bioRxiv* **2023**. doi:10.1101/2023.03.31.535084.
61. Nachury, M.V.; Weis, K. The direction of transport through the nuclear pore can be inverted. *Proceedings of the National Academy of Sciences* **1999**, *96*, 9622–9627. doi:10.1073/pnas.96.17.9622.
62. Abraham, M.J.; Murtola, T.; Schulz, R.; Páll, S.; Smith, J.C.; Hess, B.; Lindahl, E. GROMACS: High performance molecular simulations through multi-level parallelism from laptops to supercomputers. *SoftwareX* **2015**, *1-2*, 19–25. doi:10.1016/j.softx.2015.06.001.
63. Forwood, J.K.; Lange, A.; Zachariae, U.; Marfori, M.; Preast, C.; Grubmüller, H.; Stewart, M.; Corbett, A.H.;

Kobe, B. Quantitative Structural Analysis of Importin-β Flexibility: Paradigm for Solenoid Protein Structures. *Structure* **2010**, *18*, 1171–1183. doi:10.1016/j.str.2010.06.015.

64. Isgro, T.A.; Schulten, K. Binding Dynamics of Isolated Nucleoporin Repeat Regions to Importin-β. *Structure* **2005**, *13*, 1869–1879. doi:10.1016/j.str.2005.09.007.
65. Rajoo, S.; Vallotton, P.; Onischenko, E.; Weis, K. Stoichiometry and compositional plasticity of the yeast nuclear pore complex revealed by quantitative fluorescence microscopy. *Proceedings of the National Academy of Sciences* **2018**, *115*, E3969–E3977. doi:10.1073/pnas.1719398115.
66. Best, R.B.; Hummer, G.; Eaton, W.A. Native contacts determine protein folding mechanisms in atomistic simulations. *Proceedings of the National Academy of Sciences* **2013**, *110*, 17874–17879. doi:10.1073/pnas.1311599110.
67. Galvanetto, N.; Ivanović, M.T.; Chowdhury, A.; Sottini, A.; Nüesch, M.F.; Nettels, D.; Best, R.B.; Schuler, B. Extreme dynamics in a biomolecular condensate. *Nature* **2023**, *619*, 876–883. doi:10.1038/s41586-023-06329-5.

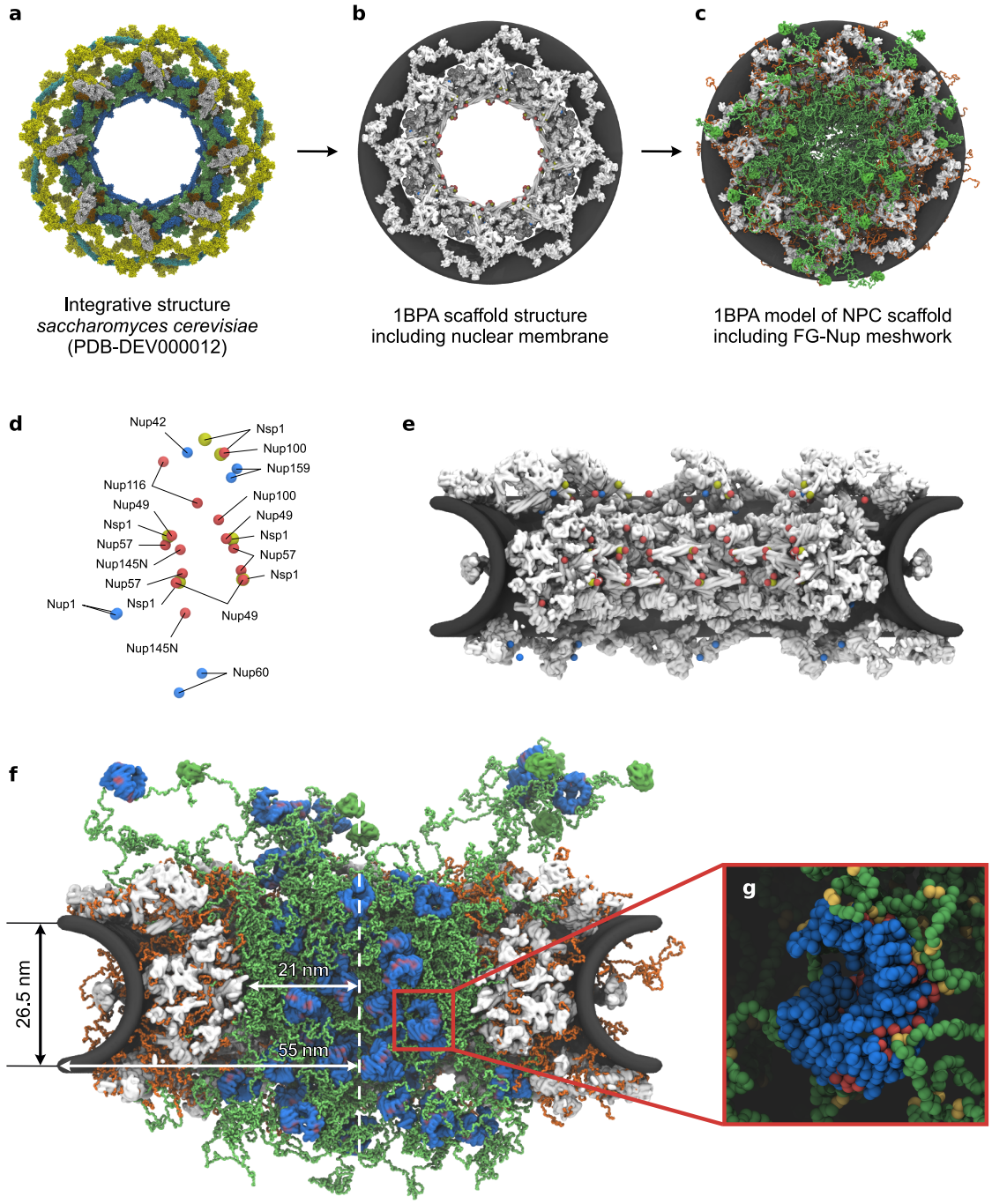

Fig. 1. Residue-scale model derived from an integrative structure of the yeast NPC. (**a**) All-atom reference structure of the yeast NPC [11]. The scaffold structure, membrane placement and disordered FG-Nup anchoring coordinates in our residue-scale model are all derived from this structure. The coloring scheme follows a grouping as defined in the original study [11]. (**b**) Residue-scale scaffold structure (white), including a torus-shaped occlusion (dark gray) that mimics the nuclear membrane. GLFG-Nup anchoring sites are indicated in red, FG-Nup anchoring sites are indicated in blue (FG-Nups: Nup159, Nup42, Nup1, Nup60) and Nsp1 anchoring sites are yellow. (**c**) A self-avoiding pseudo-random walk is used to generate missing loops in the scaffold structure (orange) and configurations of disordered FG-Nup segments (green), thus completing the residue-scale model of the yeast NPC. (**d**) Anchoring sites of individual GLFG-Nups (red), FG-Nups (blue) and Nsp1 (yellow) for a single spoke, including stoichiometry. (**e**) FG/GLFG-Nup anchoring sites (side-view), highlighting four out of eight symmetric NPC spokes. (**f**) Side-view and geometric details of the single-residue computational model of the yeast NPC including NTRs (Kap95, blue), following the coloring scheme of (c). The folded domains in the FG-Nup meshwork (green surface structures) are the β-propellers at the N-termini of the Nup159 FG domains. (**g**) Zoom in on the amino-acid details of a single Kap95 protein (blue) with binding sites (red) in the FG-meshwork (green) featuring FG-motifs (yellow). Not shown: the blue beads include cationic, anionic and aromatic residues, while the green beads include all 20 residues.

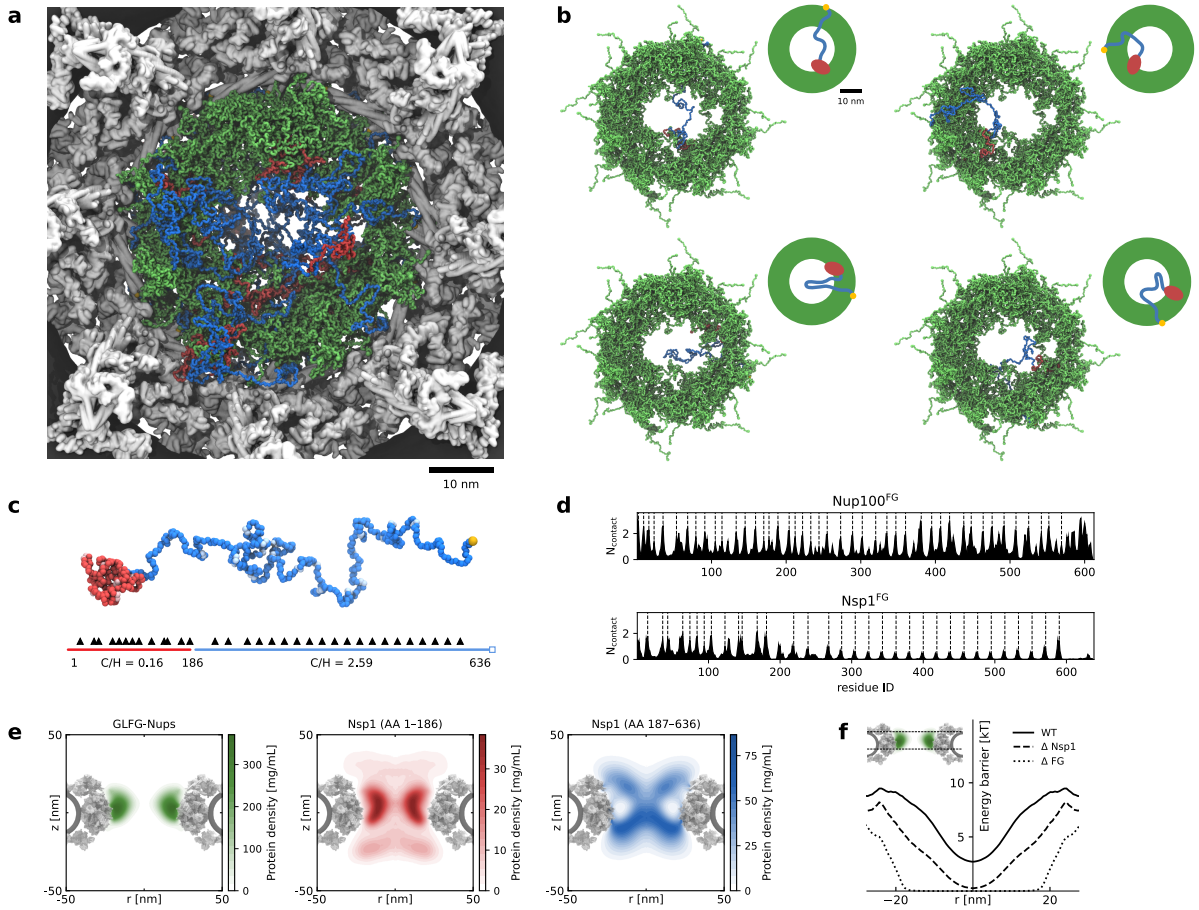

Fig. 2. The dynamic permeability barrier of the NPC. (**a**) Top view of the pore's central channel. The GLFG-Nups (green) form a ring-like assembly near the pore's scaffold. The center of this GLFG-condensate is filled by a low density percolation, formed mainly by the extended domains of Nsp1 (blue). Nsp1 molecules are anchored to the scaffold at their C-terminal (yellow), while the cohesive N-terminal domains (red) interact with the GLFG-Nups. Cytoplasmic and nucleoplasmic Nups are not shown. (**b**) Examples of individual Nsp1-proteins in the center of the pore. In all cases, the extended domain protrudes from the GLFG-condensate towards the center of the pore, while the collapsed domain sticks to this GLFG-condensate. (**c**) Bimodal structure of Nsp1 highlighted by a cohesive collapsed domain (red) and a noncohesive extended domain (blue). FG-motifs in the respective domains are highlighted by light red and blue beads; the anchor to the NPC scaffold is highlighted in yellow. The relative location of FG-motifs along the Nsp1-sequence is shown by the black markers below the protein structure. (**d**) Time-averaged number of intermolecular contacts of the FG domains of Nup100 and Nsp1 with all other Nups in the NPC (FG domains only). The dashed lines indicate the location of FG-motifs. Intermolecular contact maps for all other FG-Nup species in the pore are shown in Suppl. Fig. S3. (**e**) Radially-averaged density distributions of the GLFG-Nups and both domains of Nsp1, demonstrating that the cohesive N-terminal domain of Nsp1 primarily localizes around the GLFG-ring. (**f**) The energy barrier for passive translocation at the center of the pore for the full NPC (WT), when Nsp1 is removed (Δ Nsp1) and when all FG domains are removed (Δ FG). The inset of the NPC scaffold with GLFG-Nups shows the region that is used for analysis. Note that the analysis considers the same simulation trajectory in all three cases; the Nup deletions are done during post-processing.

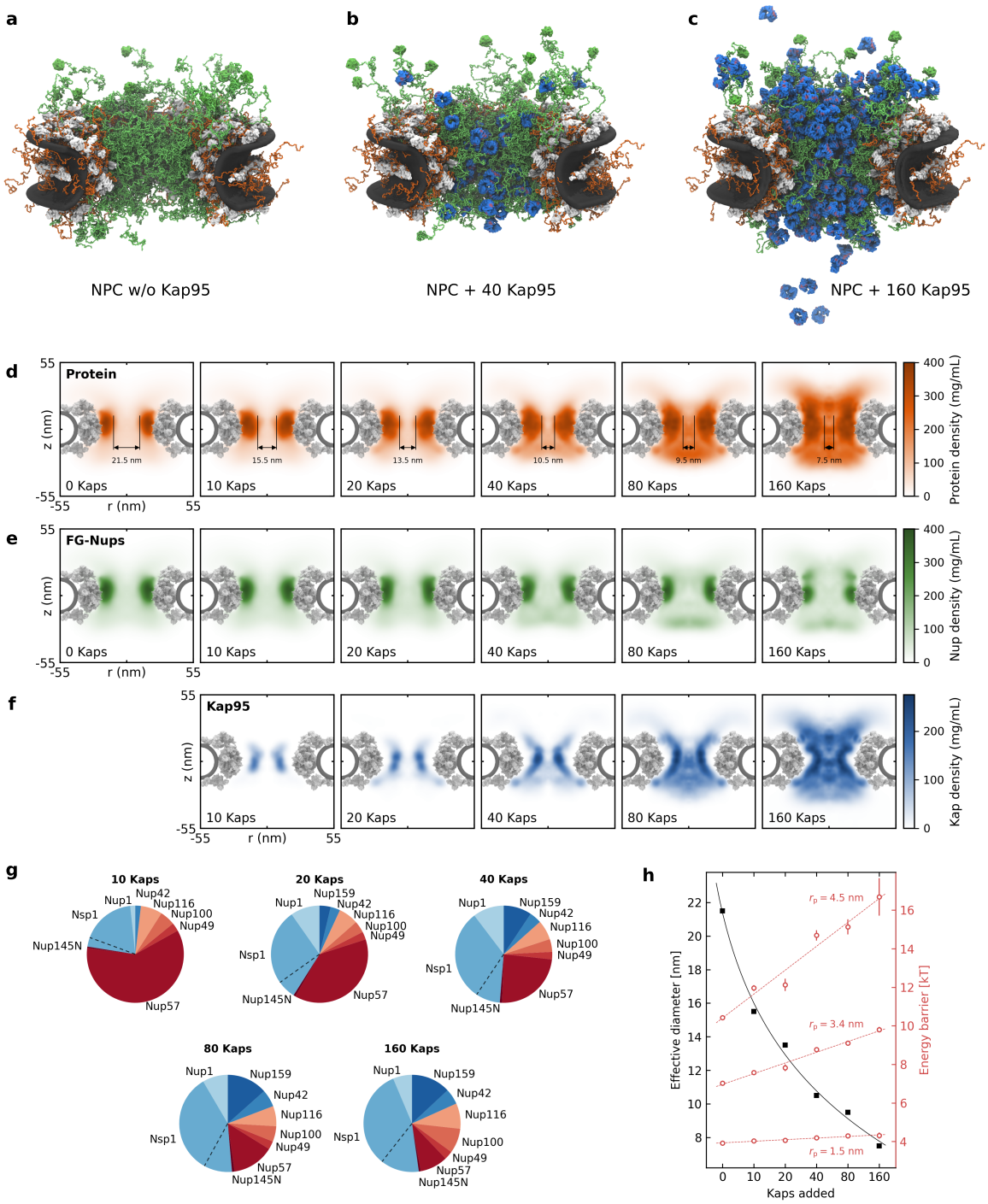

Fig. 3. Effect of Kap concentration on the FG-Nup meshwork in the NPC. (**a–c**) Simulation snapshots of the yeast NPC (a) in the absence of Kap95, (b) with 40 Kap95 proteins, and (c) with 160 Kap95 proteins. (**d**) Radially-averaged distribution of the total protein density (Nup and Kap95) in the NPC at varying concentrations of Kap95. With increasing concentration Kaps start coating the GLFG-ring, thus effectively decreasing the diameter of the low density region in the center. (**e**) Radially-averaged FG-Nup density distribution in the NPC at varying concentrations of Kap95. (**f**) Radially-averaged Kap95 density distribution in the NPC at varying concentrations of Kap95. (**g**) Relative fractions of FG-Nup–Kap interactions by FG-Nup type. At low Kap concentrations, the Kaps primarily interact with the GLFG-Nups (red). At higher Kap concentrations Kaps interact mainly with the other Nups (blue). (**h**) Kap95 crowding reduces the effective diameter of the (passive) transport channel resulting in a high selectivity for large inert cargoes. The effective diameter of the transport channel as a function of the number of Kaps added to the NPC (black squares) and the energy barrier for (passive) translocation for particles with a radius of 1.5 nm (e.g. ubiquitin), 3.0 nm (e.g. BSA) and 4.5 nm (red circles).

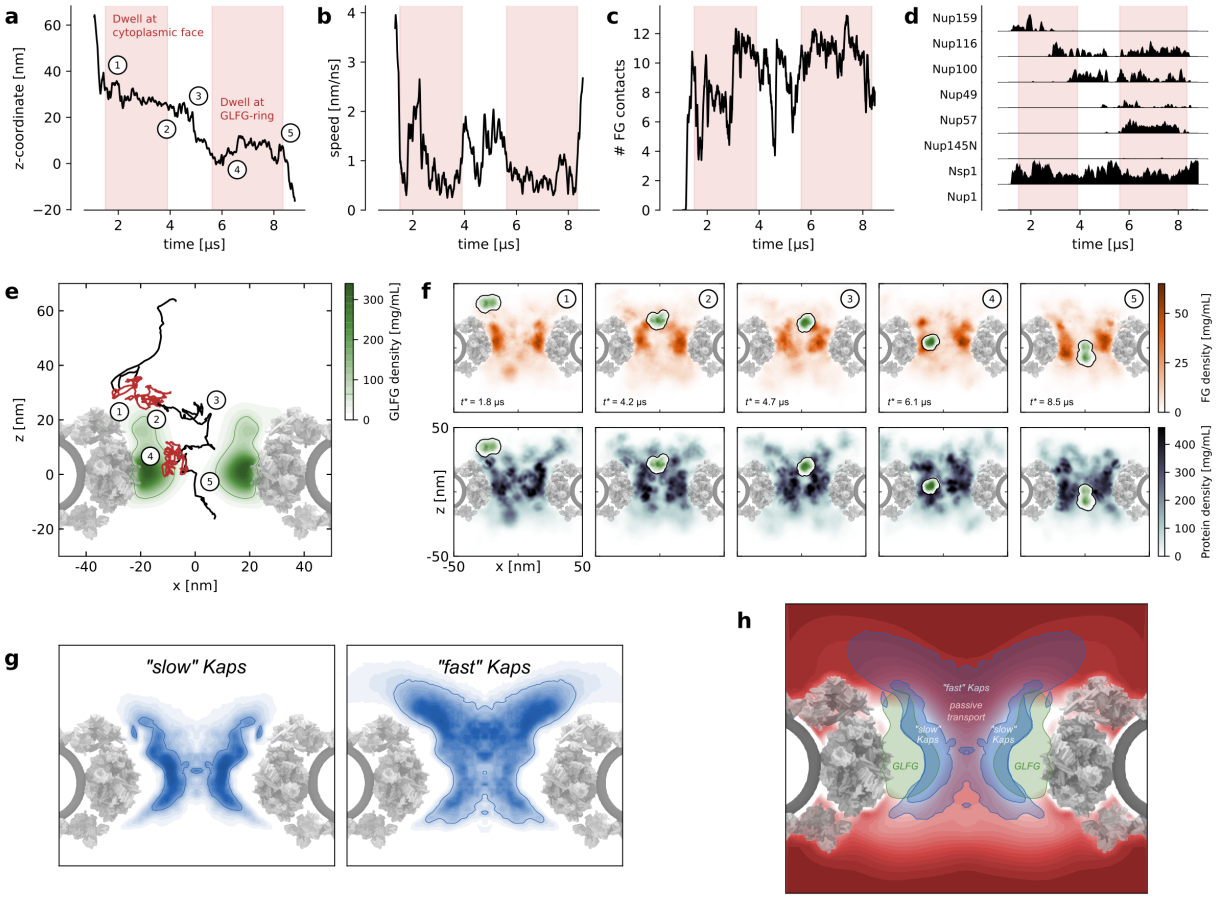

Fig. 4. Kap dynamics is described by FG-motif density and available space (steric hindrance). (**a**) Position of a selected Kap along the pore axis as a function of time. The Kap does not translocate in one go, rather it dwells at several locations in the pore (red time intervals). (**b**) Speed of the selected Kap as function of time, where the speed is measured as the displacement over a time window of 1000 ns. (**c**) Number of FG-interactions that the selected Kap experiences as a function of time. (**d**) Contacts per FG-Nup type. (**e**) Trajectory of the selected Kap, shown on top of the average density distribution of the GLFG-Nups. The color of the trajectory corresponds to the time intervals highlighted in (**a-d**). (**f**) Selected simulation snapshots of the selected Kap overlayed on top of the FG-motif distribution (top row) and the overall protein distribution (bottom row). The complete translocation event is shown in Movie 1. (**g**) Number distribution of the slower and faster Kaps. (**h**) Proposed translocation mechanism: The GLFG-Nups form a dense ring-like structure at the center of the pore (green). Kaps translocate the NPC via a “dirty velcro” mechanism: This GLFG-ring is coated by Kaps that, due to the sticky interactions of the FG-motifs, display relatively small displacements. This coating shields other Kaps from the sticky FG-interactions, allowing them to rapidly translocate through center of the pore. Passive translocation of small inert molecules (red) also occurs primarily through the center of the pore (Fig. 2f). Note that the CT is highly dynamic; average density distributions do not show the complete picture.